Crystal Structure Transformations of a Magnetoresistive La$_{0.8}$MnO$_{3-\delta}$ Thin Film

H. Vincent,[1] M. Audier, S. Pignard, G. Dezanneau, and J. P. Sénateur

LMGP (CNRS UMR 5628), ENS de Physique de Grenoble, 38402 St. Martin d'Heres, France

Structural transformations of an epitaxial La$_{0.8}$MnO$_{3-\delta}$ thin film deposited on MgO (100) substrate by metal-organic chemical vapor deposition were conjointly studied by X-ray diffraction using a conventional 4-circles-diffractometer and by transmission electron microscopy. As reported in a previous work [Pignard *et al.*, *J. Appl. Phys.*, **82**(9), 4445 (1997)] changes of physical properties of this material have been observed through annealing treatments: Films deposited at 650°C exhibit temperatures of semiconductor-metal and para-ferromagnetic transitions at 130 and 200 K while after successive annealings between 600 and 800°C in air, these transition temperatures increase up to 310 and 330 K, respectively. Two different film structures related to the evolution of these properties were determined at room temperature in their paramagnetic state. As a result, the film structures were found to be monoclinic and arranged in twinned microdomains. Several structural transformations resulting of annealing treatments were deduced: (i) The as-deposited film is almost single-phased with a *I2/b* space group structure and transforms into a mixing of two phases of *I2/b* and *P2$_1$/a* space groups in a 82/18% ratio, respectively; (ii) Mn octahedra become more regular, with significant increases of Mn–O–Mn bond angles, close to 180°. These structural changes are interpreted in a discussion related to an increase of the Mn^{4+}/Mn^{3+} ratio. Besides, as a surprising feature, observations by transmission electron microscopy on La$_{0.8}$MnO$_{3-\delta}$/MgO interfaces showed that MgO exhibits domains of *F$d\bar{3}$* cubic lattice and a cell parameter twice this of normal MgO. This seems to be the result of a strain occurring between the film and the MgO substrate rather than a chemical diffusion. © 2002 Elsevier Science (USA)

I. INTRODUCTION

Lanthanum Manganese oxide and derived compounds have been of great interest since Wollan and Koehler's pioneering work on the magnetic order (1, 2). Stoichiometric LaMnO$_3$ is an insulating material that orders antiferromagnetically at 150 K. Doping with divalent cations such as Ca, Ba, or Sr oxidizes Mn^{3+} into Mn^{4+}, introducing holes in the *d* band. Hole doping increases the conductivity and permits ferromagnetic double-exchange interactions, inducing a metal–semiconductor transition associated with a ferromagnetic ordering. Zener (3) and de Gennes (4) have considered this material as a model for establishing theoretical relationships between transport and magnetic properties.

Meanwhile, the discovery of huge magnetoresistance effects associated with these transitions (5) has again aroused interest for these compounds. As reported in the literature, very different magnetoresistive behaviors seem to be related to a number of different crystal structures of cubic or pseudo-cubic symmetry. For instance, La$_{1-x}$MnO$_{3-\delta}$ compounds have been found to exhibit at least six crystalline forms: two orthorhombic, two monoclinic, one rhombohedral, and one cubic, depending on lanthanum and oxygen concentrations (6–11). A task would then be to determine relationships between physical properties and crystalline structures.

Recently, we reported on magnetoresistance properties occurring at room temperature of epitaxial lacunar La$_{1-x}$MnO$_{3-\delta}$ thin films (0.1 ≤ *x* ≤ 0.25) obtained for the first time by metal–organic chemical vapor deposition (MOCVD) (12–14). Epitaxial films deposited on MgO, LaAlO$_3$, and SrTiO$_3$ single crystals have, whatever the *x* value, an apparent cubic symmetry with a cell parameter twice that of the normal perovskite (i.e., *a* ≈ 2 × 3.89 Å). For *x* = 0.20, films deposited at 650°C exhibit semiconductor–metal and para-ferromagnetic transitions at *T$_\rho$* = 130 K and *T$_c$* = 200 K, respectively; these transition temperatures increase up to 310 and 330 K after successive annealings between 600 and 800°C in air. In this case, annealed films present at room temperature and in low magnetic fields, one of the best magnetoresistive sensitivity (50% per Tesla in the 0–0.1 T range).

In this article we report results on crystallographic studies of La$_{0.80}$MnO$_{3-\delta}$ films before and after an annealing treatment in order to determine what structural changes can be related to temperature variations of their magnetic and

---

[1] E-mail: vincent@inpg.fr.

resistivity transitions. The different sections of the this paper are organized as follows. Sample preparations and experimental procedures are reported in Section 2. Results on structural studies are successively related to three parts in Section 3: (i) lattices determinations and space group choices, (ii) investigations by transmission electron microscopy on epitaxy relationships and space groups, and (iii) structure determinations from refinements of X-ray diffraction data. The structural changes resulting from an annealing treatment (and related to a change of magnetic and resistivity properties) are discussed in Section 4. They are interpreted as due to an increase of the $Mn^{4+}/(Mn^{3+} + Mn^{4+})$ ratio. A particular structural feature exhibited by the MgO substrate in contact with $La_{0.80}MnO_{3-\delta}$ films is also presented in Section 3 and interpreted in Section 4.

II. EXPERIMENTAL

Among cell parameter misfits of epitaxial $La_{1-x}MnO_{3-\delta}$ films with different substrates (e.g., misfits of 0.5% with $SrTiO_3$ (100), 2.5% with $LaAlO_3$(012), and 7.6% with MgO(100)), films deposited on MgO (100) substrate were chosen for X-ray diffraction studies because of larger film–substrate reflection separations in this case. A $La_{0.80}MnO_{3-\delta}$ (or LMO) film of 2 μm thickness, was deposited at 650°C on 1×1 cm^2 of the (100) face of a MgO single crystal by means of a new process of metal-organic chemical vapor deposition called "Injection-MOCVD" (15). Experimental details about the CVD-reactor, precursor dilutions, gas flows, and temperature–pressure conditions have been given in a previous article (12) related to a study of physical properties of such LMO films. Using $LaAlO_3$ and Mn_2TiO_4 compounds as standards, the composition of the thin film was determined by X-ray wavelength dispersive spectroscopy on a Cameca SX50 microprobe. The chemical formula of films was found to be $La_{0.80(\pm0.02)}Mn_{1.00(\pm0.02)}O_{3-\delta}$. However the oxygen concentration could not be determined due to the influence of the MgO substrate; thus the oxygen deficiency δ in the $La_{0.80}MnO_{3-\delta}$ formula stands as an undetermined parameter. No foreign phase has been observed either by SEM or TEM. The MgO substrate thickness was reduced down to 200 μm by polishing. The sample was cut in two parts and one of them was annealed at 700°C for 3 h in air. Temperature dependences of magnetization (under a constant field of 0.2 T) and electrical resistance (at zero field) for both as-deposited and annealed films were measured using a vibrating sample magnetometer and a four probes method, respectively. As shown in Fig. 1, the temperatures of magnetic (T_c) and electrical (T_ρ)) transitions change from 210 to 295K and from 130 to 265 K, respectively (T_ρ is defined at the maximun of resistivity). As our crystallographic studies were carried out at room temperature (293 K), the samples were in a paramagnetic state according
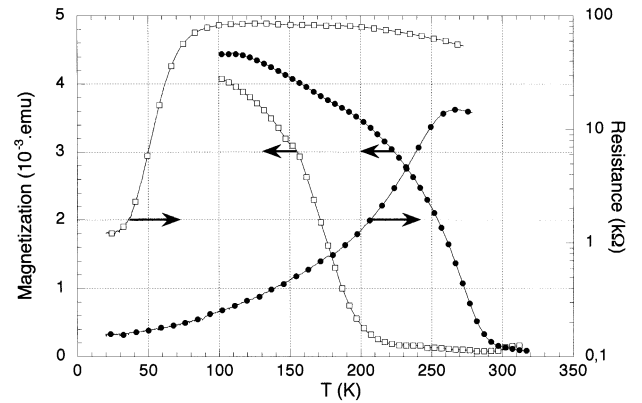

FIG. 1. Magnetization and resistance versus temperature for as-deposited and annealed $La_{0.80}MnO_{3-\delta}$ films (empty square dots for the as-deposited film and black circle dots for the annealed film).

to the magnetic curves observed in Fig. 1. For X-ray data collections, sample pieces of 1×1 mm^2 were mounted in reflection geometry on a Nicolet 4-circles diffractometer with graphite-monochromated Mo$K\alpha$ radiation ($\lambda = 0.7107$ Å) and a counter aperture of 4°. Intensities of more than 5000 reflections were measured on both as-deposited and annealed LMO films, in a range $2\theta = 70°$ with ω-scan mode in an half Ewald sphere (see Table 1 for details). Reflections either too close to those of the MgO substrate or corresponding to incident or diffracted beams not enough inclined with respect to the film surface were not considered. Absorption corrections based on an experimental Ψ-scan method were carried out. Finally a total of more than 700 reflections with a cutoff of $F^2 \geq 2$ were used for refinements. For investigations by transmission electron microscopy (TEM), samples were prepared by scraping small fragments from the rest of films on their MgO substrate which were deposited onto copper grid coated with a carbon film. A JEOL 200CX microscope was used in a configuration allowing large tilt angles of the specimen ($\pm 45°$) and a lattice fringe resolution of 3.2 Å.

III. RESULTS

III.1. Lattice and Space Groups

Lattice parameters of LMO films were first determined from 50 reflections centered at high 2θ angles ($40° \leq 2\theta \leq 60°$). The overall symmetry was found to be cubic for both samples with a unit cell parameter twice that of the classical perovskite (Table 1). The unit cell is slightly smaller after annealing.

Among all the collected reflections, most of them (85%), and in particular those of strong intensity, belong to a F lattice. However, as no systematic extinction was observed, different space groups could be assumed.

TABLE 1
Experimental Conditions for X-Ray Data Analyses and Measured Cell Parameters on As-Deposited and Annealed La$_{0.80}$MnO$_{3-\delta}$ Films

		as-deposited film	annealed film
Sample size (μm)		$1000 \times 1000 \times 2$	$1000 \times 1000 \times 2$
Number of measured reflections		5357	6101
Scan mode		ω-scan	
Scan width		5.0°	
FWHM		$\Delta\omega \approx 1.6°$(instrumental resolution 0.25°)	
Measured ranges:			
	2θ	$3 \leq 2\theta \leq 70$	
	h	$-12 \leq h \leq 12$	
	k	$-12 \leq k \leq 12$	
	l	$0 \leq l \leq 12$	
Period of intensity control		100 reflections	
Absorption correction		ψ-scan	
μ(MoKα) (cm^{-1})		195.8	
Observed reflections $(F^2/\sigma(F^2)) \geq 2$		701	757
Refinement program		M.X.D. (23)	
Refined parameters		39	
Weighting scheme		$w = 1/\sigma^2(F^2)$	
Measured cell parameters:			
	a (Å)	7.766(3)	7.758(3)
	b (Å)	7.767(3)	7.761(3)
	c (Å)	7.767(3)	7.760(3)
	α	89.98(3)°	90.02(3)°
	β	89.94(3)°	90.02(3)°
	γ	90.01(3)°	90.01(3)°

When looking for a space group, it is useful to consider the tilt-system nomenclature proposed by Glazer for the perovskite-like structures (16–18). Tilting of the octahedra causes doubling of the unit-cell axes. Glazer's symbols are given for each tilt system by three letters *a*, *b*, *c* with superscripts + or − or 0. Letters refer to octahedra tilting about the three ⟨100⟩ directions of the pseudo-cubic cell; a repetition of letter (e.g., *a a a*) denotes equality of tilt magnitude; superscripts + or − or 0 mean that the octahedra along the tilt axis are either tilted *in phase* or *antiphase* or *not tilted* about this axis. Six tilt systems are compatible with a *F* lattice after doubling the cubic cell of the aristotype perovskite, and six other tilt systems are compatible with *A*- or *B*-face centered cells (Table 2). When twinning these last systems in the three space directions, a pseudo *F* cubic lattice can be generated considering only the strong reflections (actually no tilt system of cubic symmetry agrees with a double perovskite *F* cubic cell). In the notation of tilt systems considered in the present work, the monoclinic axis is the **c** axis and the large axis of the pseudo-orthorhombic cell is the **b** axis.

Among all these systems, only three with space groups $I2/b$, (no. 15), $R\bar{3}c$ (no. 167), and $Pnma$ (no. 62) have been proposed for the description of LMO crystal structures (6–11). Therefore, considering only these three space groups and all possibilities of twinned arrangements, we have performed preliminary structural refinements using SHELX-93 program (19). The best result was obtained with the $I2/b$ space group. Then, in order to improve a determination of structural models, in particular models based on the coexistence of several structures of different space groups, the following results of TEM investigations on space groups and twinning of LMO films were considered afterward in refinements.

III.2. T.E.M. Analysis

TEM investigations on space groups, crystallographic orientations, and LMO/MgO epitaxy relationships have required examination of several selected area diffraction patterns associated with bright and dark field images and related through different rotations to a same domain observed in a sample fragment.

III.2.a. Annealed LMO film. Two phases have been evidenced in the annealed LMO film. Both are monoclinic with $\beta = 90°$ and compatible with $P2_1/a$ and $I2/b$ space groups. Careful analyses of electron diffraction were however required as both these space groups might respectively be confused with those of orthorhombic $Pnma$ and rhombohedral $R\bar{3}c$ systems because of dynamical electron diffraction effects. For instance, on account of double diffraction effects, both $Pnma$ and $P2_1/a$ space groups cannot be distinguished from reflections observed on the three patterns shown in Fig. 2a. These selected area diffraction patterns are related by rotations around the $h0h$ reflection row of a same crystalline domain. From reflection conditions of $Pnma$

TABLE 2
Glazer's Tilt Systems Compatible with Face Centered Double Cell Cubic Perovskite: (a) *F* Lattice Centering; (b) *A* (or *B*) Lattice Centering

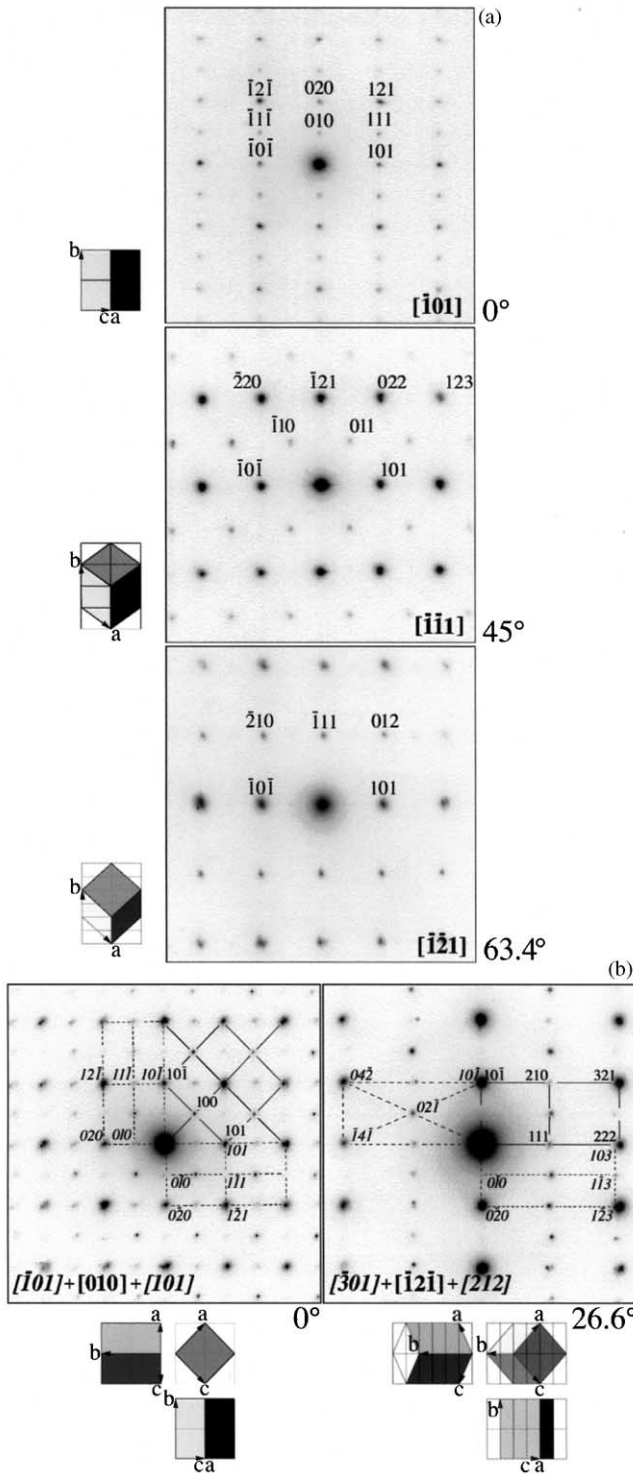| System no.	Symbol	Space group
(a)		
12	a$^-$b$^-$c$^-$	$F\bar{1}$
13	a$^-$b$^-$b$^-$	$I2/a$
14	a$^-$a$^-$a$^-$	$R\bar{3}c$
19	a^{0}b$^-$c$^-$	$F2/m$
20	a^{0}b$^-$b$^-$	$Imcm$
22	a^{0}a^{0}c$^-$	$F4/mmc$
(b)		
8	a$^+$b$^-$c$^-$	$A2_1/m$
9	a$^+$a$^-$c$^-$	$A2_1/m$
10	a$^+$b$^-$b$^-$	$Pmnb$
11	a$^+$a$^-$a$^-$	$Pmnb$
17	a^{0}b$^+$c$^-$	$Bmmb$
18	a^{0}b$^+$b$^-$	$Bmmb$

FIG. 2. (a) Selected area diffraction patterns related by rotations around the $h0h$ reflection row of a same crystalline domain (both $Pnma$ and $P2_1/a$ space groups cannot be distinguished from reflections observed on these patterns because of double diffraction effects); (b) Diffraction patterns corresponding to a crystal structure formed of microdomains with 3 different orientations and related by a rotation of 26.6° around the vertical row of reflections (and used for the $P2_1/a$ space-group identification (see text)).

($h = 2n$ for $hk0$, $k + l = 2n$ for $0kl$) all forbidden reflections such as 010 on the pattern of $[\bar{1}01]$ zone axis, $\bar{1}10$ and 011 on the pattern of $[\bar{1}\bar{1}1]$ zone axis, $\bar{2}10$ and 012 on the pattern of $[\bar{1}\bar{2}1]$ zone axis, might be the result of a double diffraction between permitted reflections (e.g., $\mathbf{g}_{010} = \mathbf{g}_{11\bar{1}} + \mathbf{g}_{111}$). Considering the less restricted conditions of $P2_1/a$ ($h = 2n$ for $hk0$ and $l = 2n$ for $00l$), double diffraction effects can as well be considered for all the forbidden reflections of the type 010, $\bar{1}10$, and $\bar{2}10$. Therefore, it was necessary to verify in this case what are the conditions on $hk0$ and $0kl$ reflections which cannot be the result of double diffraction effects for at least one of these space groups. The choice for the $P2_1/a$ space group was made from an indexing of diffraction patterns corresponding to a crystal structure formed of microdomains with 3 different orientations (Fig. 2b). These orientations are related to a pseudo double cubic cell by matrices of the type

$$\begin{bmatrix} \mathbf{a_m} \\ \mathbf{b_m} \\ \mathbf{c_m} \end{bmatrix} = \begin{bmatrix} \frac{1}{2} & 0 & -\frac{1}{2} \\ 0 & 1 & 0 \\ \frac{1}{2} & 0 & \frac{1}{2} \end{bmatrix} \begin{bmatrix} \mathbf{a_c} \\ \mathbf{b_c} \\ \mathbf{c_c} \end{bmatrix}$$
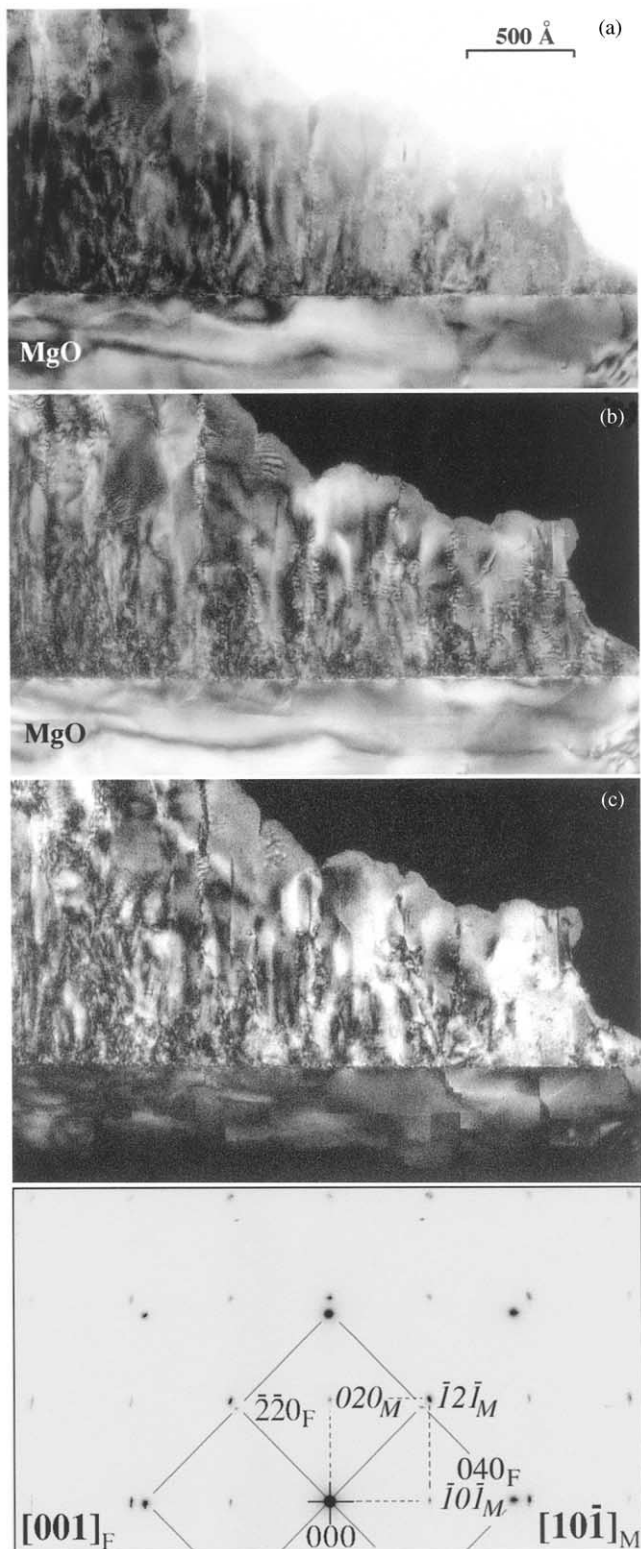
and related matrices corresponding to the various cubic cell settings ($\mathbf{b_c c_c a_c}$, $\mathbf{c_c a_c b_c}$, $\mathbf{a_c b_c} -\mathbf{c_c}$, $\mathbf{b_c} -\mathbf{c_c a_c}$, and $-\mathbf{c_c a_c b_c}$) where the subscripts "m" and "c" stand for monoclinic and pseudo-cubic cells respectively. Both diffraction patterns shown in Fig. 2(b) are related by a rotation of 26.6° around the vertical row of reflections (i.e. an angle corresponding to this formed between [210] and [100] axes in a cubic system). As proposed in Fig. 2b, an indexing of these patterns appears to be in agreement with patterns expected for a 26.6° rotation of each cell orientation. Then, it can be deduced that $02\bar{1}$ and $\bar{1}20$ reflections observed along the $[\bar{3}01]$ zone axis are both forbidden in the $Pnma$ space-group (and should not be observed in this case) while for the $P2_1/a$ space-group conditions, the $02\bar{1}$ reflection is permitted and $\bar{1}20$ forbidden but its presence can be interpreted as the result of a double diffraction (e.g., $\mathbf{g}_{\bar{1}20} = \mathbf{g}_{\bar{1}01} + \mathbf{g}_{02\bar{1}}$). Besides, as shown after, an epitaxy relationship has been observed between this monoclinic $P2_1/a$ phase and the MgO substrate.

The identification of the other phase of $I2/b$ space group was achieved from LMO crystalline domains exhibiting an interface with the MgO substrate (Figs. 3 and 4). In this case, the MgO substrate was used as a reference for carrying out different rotations of a same LMO crystal domain. However, before examining which reflection conditions lead to distinguish between both $I2/b$ and $R\bar{3}c$ space groups, let us first describe particular reflections exhibited by the MgO substrate in contact with the LMO film. Figure 3 shows bright and dark fields images and the corresponding electron diffraction pattern of a LMO/MgO cross-section oriented along a [001] zone axis of the MgO substrate. On this pattern, two sets of reflections with two different square

arrangements can be distinguished. Indexes with "F" subscript (for F lattice) are related to the MgO substrate and those with "M" subscript (for monoclinic lattice) are related to the LMO layer. However, instead of reflections related to

FIG. 3. Bright and dark fields images and corresponding electron diffraction pattern of a LMO/MgO cross-section oriented along a [001] zone axis of the MgO substrate. The diffraction pattern exhibits two sets of reflections with two different square arrangements corresponding to the MgO substrate (indexes with subscripts "F") and to the LMO layer (indexes with subscripts "M"). Instead of reflections related to the normal $Fm\bar{3}m$ space group of the MgO structure ($a = 4.217$ Å) additional reflections are observed to be characteristic of either a $Fd\bar{3}$ or $Fd\bar{3}m$ space group and a cubic cell parameter twice this of the normal MgO structure. MgO domains corresponding to this particular cell are identified from a comparison of both dark field images: The first dark field image (b) obtained by selecting both 040_M and 400_F reflections shows a complete illumination of the MgO substrate while the dark field image (c), obtained by selecting both $\bar{1}2\bar{1}_M$ and $\bar{2}20_F$ reflections shows illuminated MgO domains on about 400 Å thickness from the interface and which structure is characteristic of a $Fd\bar{3}$ or $Fd\bar{3}m$ space group. Wall boundaries mainly extending along {100} planes are observed in between these domains (probably antiphase boundaries) and as an interface with the standard MgO structure.

the $Fm\bar{3}m$ space group of the MgO structure ($a = 4.217$ Å) additional reflections were found through different rotations of this sample to be characteristic of either $Fd\bar{3}$ or $Fd\bar{3}m$ space group, the cubic cell parameter being twice this of the normal MgO structure (see also Fig. 4). MgO domains corresponding to this particular cell were identified from a comparison of dark field images. The first dark field image in Fig. 3b obtained by selecting both 040_M and 400_F reflections shows a complete illumination of the MgO substrate; but the dark field image Fig. 3c, obtained by selecting both $\bar{1}2\bar{1}_M$ and $\bar{2}20_F$ reflections shows illuminated MgO domains on about 400 Å thickness from the interface which structure is characteristic of a $Fd\bar{3}$ (or $Fd\bar{3}m$) space group. Wall boundaries mainly extending along {100} planes are observed in between these domains (probably antiphase boundaries) and as an interface with the standard MgO structure. A priori, such a structural change could be due either to a chemical diffusion from the LMO layer within the MgO substrate or to a constraint existing at the interface with the LMO film.

From bright and dark fields images shown in Fig. 3, the LMO film exhibits a columnar texture. Some variations in the contrast and moiré fringes are characteristic of a few lattice distortions resulting in the existence of subgrain boundaries between columns. A space group $I2/b$ was verified from a set of several selected area electron diffraction patterns (selected area of about 3500 Å diameter) related through different rotations to the same sample domain as the domain shown in Fig. 3 (i.e., constituted of several columns). In Fig. 4a, both patterns of $[10\bar{1}]_M$ and $[11\bar{1}]_M$ zone axes, related by a 45° rotation around the $h0h_M$ row, correspond to the LMO/MgO interface in edge-on position with respect to the incident electron beam. A high resolution image corresponding to a part of this interface oriented along the $[11\bar{1}]_M$ zone axis is shown in Fig. 4b. The existence of a MgO structure characteristic of a double F cubic cell

parameter was confirmed from the Fourier transform diagram shown in the inset. The other patterns of $[00\bar{1}]_M$, $[31\bar{1}]_M$ and $[210]_M$ zone axes correspond to rotations of 45°

around the 0k0 row and of 35.26° and 54.74° around the $\bar{h}k\bar{h}_M$ row, respectively. They exhibit groups of very close reflections that are the result of multiple scattering effects through both the MgO substrate and the LMO layer. Due to double diffraction effects between reflections of the LMO layer, an indexing of these patterns was found to be in agreement with the reflection conditions of the $I2/b$ space group ($h + k + l = 2n$ for hkl; $h, k = 2n$ for $hk0$). The case of a rhombohedral space group $R\bar{3}c$ could be excluded by considering that both patterns of $[00\bar{1}]_M$ and $[11\bar{1}]_M$ zone axes should correspond to $[0\bar{1}0]_R$ and $[0\bar{1}1]_R$ zone axes of a rhombohedral cell. In this case, the reflection 220_M of the pattern $[00\bar{1}]_M$ should be indexed as 002_R which is in agreement with the reflection conditions of $R\bar{3}c$ ($l = 2n$ for hhl and $h = 2n$ for hhh). But the well visible $0\bar{3}3_M$ reflection of the pattern $[11\bar{1}]_M$ should be indexed $\bar{3}\bar{3}3_R$ in the rhombohedral system, which is not permitted in $R\bar{3}c$ and cannot be due to any multiple scattering phenomenon.

With respect to the MgO (100) substrate, the epitaxy of the monoclinic LMO layer is such that:

$$(101)_M // (100)_{MgO}$$

$$[001]_M // [010]_{MgO}$$

We have also observed another epitaxy relationship where:

$$(001)_M // (100)_{MgO}$$

$$[101]_M // [010]_{MgO}$$

Although in the case of the monoclinic $P2_1/a$ structure, similar epitaxy relationships were deduced from TEM observations, a few differences with respect to the case of the $I2/b$ structure were found. For instance, in Fig. 5 both diffraction patterns corresponding to a $P2_1/a$ LMO/MgO interface are related by 45° rotation around the 0k0 row of the MgO substrate. In this case, we first noticed that the MgO structure in contact with the LMO film does not transform as in the case of the $I2/b$ structure. From the pattern of $[0\bar{1}0]$ zone axis corresponding to the interface viewed in edge-on position (as indicated in the schema on the right), it appears that a very small rotation occurs between both monoclinic $P2_1/a$ LMO and cubic MgO lattices. Such a small rotation is confirmed by the fact that through the 45° rotation, small sets of multiple scattered
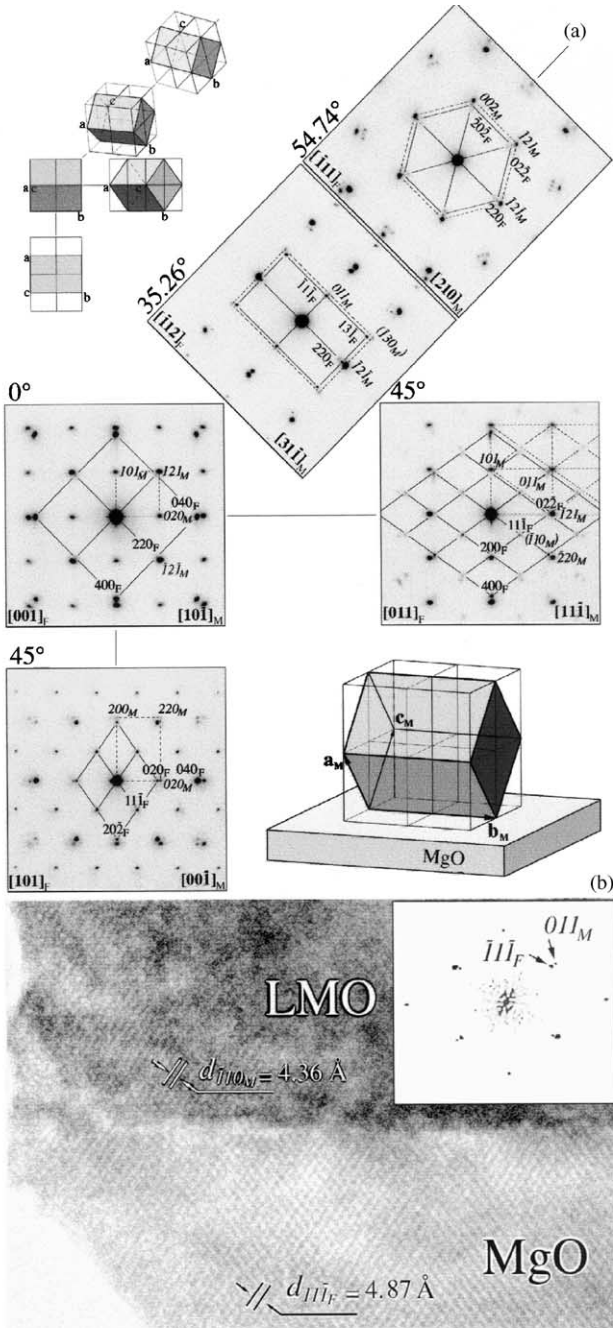
FIG. 4. (a) Set of selected area electron diffraction patterns related by different rotations of the same annealed LMO/MgO interface corresponding in part to the high resolution image shown in (b). The patterns of $[10\bar{1}]_M$ and $[11\bar{1}]_M$ zone axes related by a 45° rotation around the $h0h_M$ row correspond to the LMO/MgO interface in edge-on position with respect to the incident electron beam. The diffracting vector associated to the reflection 101_M is normal to the interface. Other patterns of $[00\bar{1}]_M$, $[31\bar{1}]_M$, and $[210]_M$ zone axes correspond to rotations of 45° around the 0k0 row and of 35.26° and 54.74° around the $\bar{h}k\bar{h}_M$ row, respectively. They exhibit groups of very close reflections resulting of multiple scattering effects through both the MgO substrate and LMO layer. Due to double diffraction effects between reflections of the LMO layer, an indexing of these patterns was found to be in agreement with the reflection conditions of the $I2/b$ space group ($h + k + l = 2n$ for hkl; $h, k = 2n$ for $hk0$). Both the 111 fringes of MgO observed on the image (b) and the Fourier transform pattern of the image (insert) confirms the structural transformation of the MgO substrate described in Fig. 3.
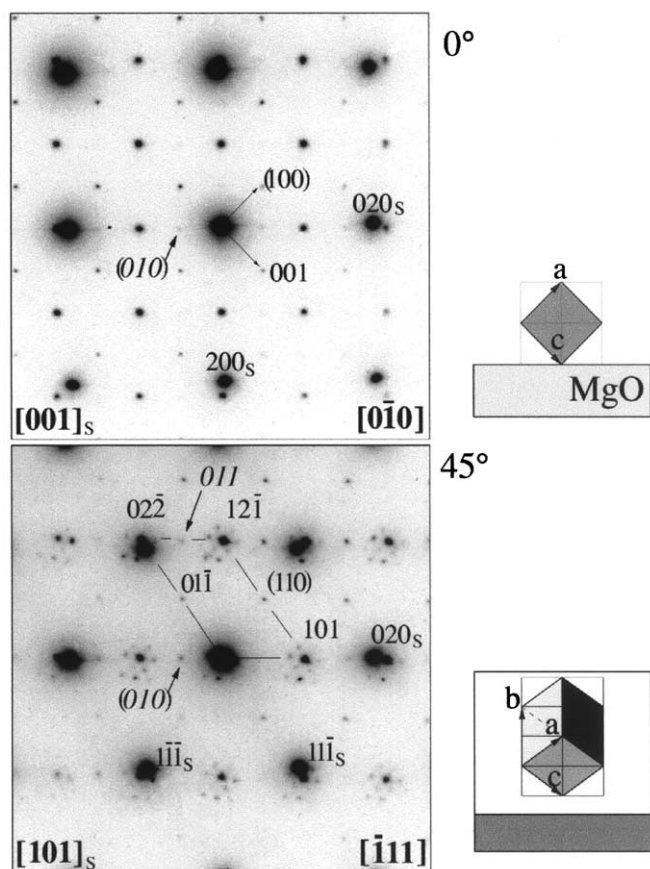
FIG. 5. Selected area electron diffraction patterns related by 45° rotation of the same LMO/MgO interface. In that case, the annealed LMO structure belongs to the $P2_1/a$ space group and the orientational relationship with the MgO substrate exhibits a small misorientation (see text).

reflections of $2mm$ symmetry are misoriented with respect to the $2mm$ symmetry of the LMO or MgO structure. Besides, from an indexing of these patterns, it appears that several reflections of very weak intensities are due to the presence of other microdomains of different orientations like those previously indicated in Fig. 2b.

III.2.b.   As-deposited LMO film. All diffraction patterns observed on the as-deposited film exhibited broad reflections which could, a priori, be considered to be typical of the F cubic system. However, as intensities of hhh ($h = 2n + 1$) reflections were also observed to be different for patterns of equivalent zone axes, the case of a F cubic system had to be excluded. For instance, both the patterns of $[11\bar{1}]_M$ and $[00\bar{1}]_M$ zone axes shown in Fig. 6 cannot be assumed to be equivalent to patterns of $\langle 110 \rangle$ zone axis in a F cubic system as they are different (i.e., equivalent hhh ($h = 2n + 1$) reflections in the F cubic system cannot be either present or absent). As a matter of fact, such features can only be interpreted on the basis of a microdomain monoclinic

structure of $I2/b$ space group (i.e., according to indexing proposed in Fig. 6). Besides, we have found that epitaxy relationships between this phase and the MgO substrate are similar to those reported before about the annealed LMO layer of $I2/b$ space group. Let us note that for all TEM observations carried out on MgO/LMO interfaces (i.e., 4 observations) we have also observed in this case a MgO structure of $Fd\bar{3}$ or $Fd\bar{3}m$ space group with a cubic cell parameter twice that of the normal MgO structure. For this
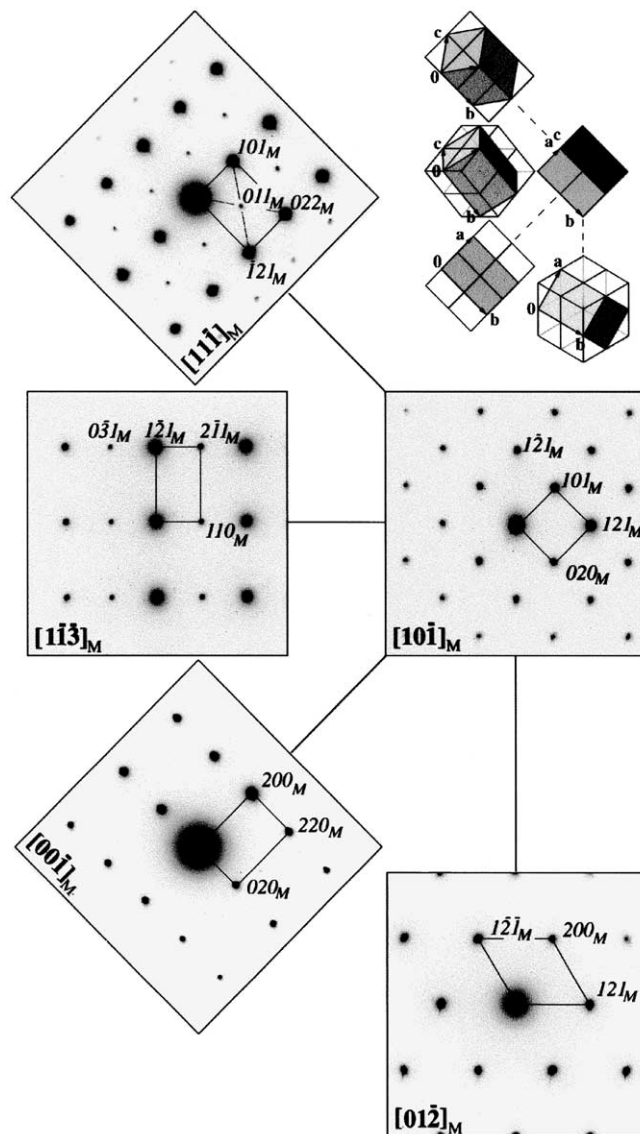
FIG. 6. Selected area electron diffraction patterns of the as-deposited LMO layer. Their indexing corresponds to that of a monoclinic structure of $I2/b$ space group. As mentionned in the text, the patterns of $[11\bar{1}]_M$ and $[00\bar{1}]_M$ zone axes cannot be assumed to be equivalent to patterns of $\langle 110 \rangle$ zone axis in a F cubic system as they are different (i.e., equivalent hhh ($h = 2n + 1$) reflections in the F cubic system cannot be at the time present and absent).

reason, we think that such a structural change of the MgO substrate would be the result of a constraint existing at the interface with the LMO structure of $I2/b$ space group rather than a chemical diffusion. Therefore, we shall propose in the discussion, a possible transformation of the MgO structure causing a doubling of its unit-cell axes and a space group $Fd\bar{3}$.

III.3. Structure Determination and Refinements

Because of these TEM results, further structural refinements were performed on different phase mixings using a versatile MXD program (20). Among the possible space groups $Pnma$, $R\bar{3}c$, $P2_1/a$, and $I2/b$, two starting models were considered: (i) one constituted of orthorhombic $Pnma$ and rhombohedral $R\bar{3}c$ structures described in the double cubic cell ($2a_0, 2a_0, 2a_0$) (in this case double cubic cells of pseudo space groups " $B2_1/m$ " and " $F\bar{3}c$ " were used in order to carry out the refinement procedure) and (ii) another one constituted of two monoclinic $P2_1/a$ and $I2/b$ structures described in an orthorhombic-like cell ($a_0\sqrt{2}, 2a_0, a_0\sqrt{2}$). Besides, different orientations of crystalline domains resulting of different twinning were systematically assumed in both these models. For the rhombohedral structure, four domain orientations related by the threefold axis successively parallel to one of the four $\langle 111 \rangle$ axes of the pseudo-cubic cell, and the 3 basis vectors **a** parallel to $\langle 110 \rangle$ cubic directions were considered. For the structures described in orthorhombic-like cells and as proposed by Moussa *et al.* (21), six domains were input: three domains orienting the large axis **b** successively along the three axes $\langle 100 \rangle$ of the cubic cell and three domains inputing the mirror planes $\{100\}$ of the cubic cell containing the orthorhombic **b** axis. Contributions of each of these domains were refined.

Because of high correlated scattering effects occurring from twinned domains and phase mixings, a particular three-steps refinement procedure was applied: (i) contributions of different domain orientations within each space group were first refined by fixing atomic positions and thermal factors at values deduced from different powder X-ray and neutron diffraction experiments on LMO samples [8–10]; (ii) all atomic position parameters were then refined with fixed isotropic thermal factor values; and (iii) these last parameters were finally refined. Population parameters were fixed at values determined from X-ray wavelength dispersive spectroscopy analyses; all oxygen occupancy factors were fixed at 1 as the oxygen deficiency δ could not be determined (cf. Section 2). Meanwhile, we have found that small variations in the oxygen occupancy factors (up to 5%) yield negligible variations on the reliability factors. Refinement results on the volume fractions of phases and reliability factors are reported in Table 3. For both samples, refinement factors ($Rw(F^2)$ and $R(F)$) appear to be significantly better for a mixing of monoclinic $I2/b$

TABLE 3
Comparaison of Results for Different Refinements

Cell	Space group	% ratio	$Rw(F^2)$	$R(F)$
(1) annealed				
	$Pnma$	39%		
$2a_0, 2a_0, 2a_0$	and		0.127	0.051
	$R\bar{3}c$	61%		
	$I2/b$	82%		
$a_2\sqrt{2}, 2a_0, a_0\sqrt{2}$	and		0.101	0.030
	$P2_1/a$	18%		
(2) as deposited				
	$Pnma$	35%		
$2a_0, 2a_0, 2a_0$	and		0.130	0.054
	$R\bar{3}c$	65%		
	$I2/b$	>95%		
$a_0\sqrt{2}, 2a_0, a_0\sqrt{2}$	and		0.111	0.041
	$P2_1/a$	<5%		

Note. In $R\bar{3}c$, described in the double cubic cell, the general position (multiplicity 48) can be writen: (x, y, z) (z, x, y) (y, z, x) $(-x + \frac{1}{2}, -z + \frac{1}{2}, -y + \frac{1}{2})$ $(-z + \frac{1}{2}, -y + \frac{1}{2}, -x + \frac{1}{2})$ $(-y + \frac{1}{2}, -x + \frac{1}{2}, -z + \frac{1}{2})$ $(-x, -y, -z)$ $(-z, -x, -y)$ $(-y, -z, -x)$ $(x - \frac{1}{2}, z - \frac{1}{2}, y - \frac{1}{2})$ $(z - \frac{1}{2}, y - \frac{1}{2}, x - \frac{1}{2})$ $(y - \frac{1}{2}, x - \frac{1}{2}, z - \frac{1}{2})$ and $(0, 0, 0) +$, $(0, \frac{1}{2}, \frac{1}{2}) +$, $(\frac{1}{2}, 0, \frac{1}{2}) +$ and $(\frac{1}{2}, \frac{1}{2}, 0) +$. In $Pnma$ the general position (multiplicity 16) can be writen: (x, y, z) $(\frac{1}{2} - z, \frac{1}{2} - y, -x)$ $(-x, \frac{1}{2} + y, -z)$ $(\frac{1}{2} + z, -y, x)$ $(-x, -y, -z)$ $(-\frac{1}{2} + z, -\frac{1}{2} + y, x)$ $(x, -\frac{1}{2} - y, z)$ $(-\frac{1}{2} - z, y, -x)$ and $(0, 0, 0) +$ and $(\frac{1}{2}, 0, \frac{1}{2}) +$.

$+$ $P2_1/a$ structures than for this of $R\bar{3}c + Pnma$. Then it can be deduced that the annealing treatment increases the proportion of the phase with $P2_1/a$ space group (from less than 5% up to 18%) and modifies atomic coordinates (Table 4) such that tilt angles between octahedra become close to 180° (Table 5). The thermal factors of all atoms are very high but they cannot be considered significant because of the structural arrangement in twinned microdomains; their high values represent a position disorder between domains and not high thermal vibrations. Thermal factors can also be anormaly high because of inaccuracies in absorption corrections at low theta angle in the case of a thin film geometry.

IV. DISCUSSION

In summary, detailed structural information were obtained from refinements of X-ray diffraction data for which structural features studied by TEM were considered. Structural transformations of an epitaxial $La_{0.80}MnO_{3-\delta}$ thin film are precised in relation to changes of physical properties obtained through an annealing treatment at 700°C for 3 h in air. The changes of the film structure result (i) in the formation of a secondary phase of $P2_1/a$ space group, (ii) of different proportions of microdomain orientations with respect to the MgO substrate, and (iii) of different Mn–O and La–O bound distances and tilt angles between octahedra.

TABLE 4
Structural Parameters Observed before and after Annealing

(1) Before annealing
$I2/b$ space group
Weigth of each oriented domain: 0.37(8), 0.25(8), 0.30(8), 0.07(9), 0.00(9), 0.02(9)

Atoms	Positions	x	y	z	u (Å^2)
La	4e	0	$\frac{1}{4}$	0.4986(5)	0.029(1)
Mn	4a	0	0	0	0.028(1)
O(1)	4e	0	$\frac{1}{4}$	0.0290(12)	0.042(2)
O(2)	8f	0.2821(9)	$-$0.0079(7)	0.2076(10)	0.043(3)

(2) After annealing
(a) major phase (wt 82%), $I2/b$ space group
Weigth of each oriented domain: 0.18(7), 0.21(3), 0.15(7), 0.12(7), 0.00(9), 0.16(7)

Atoms	Positions	x	y	z	u (Å^2)
La	4e	0	$\frac{1}{4}$	0.5052(4)	0.024(1)
Mn	4a	0	0	0	0.031(1)
O(1)	4e	0	$\frac{1}{4}$	0.0015(11)	0.016(2)
O(2)	8f	0.2682(12)	0.0015(9)	0.2427(13)	0.034(3)

(b) minor phase (wt 18%), $P2_1/a$ space group Weigth of each oriented domain: 0.04(1), 0.00(2), 0.05(1), 0.05(1), 0.03(1), 0.03(1)

Atoms	Positions	x	y	z	u (Å^2)
La	4e	0.0131(6)	0.2528(5)	0.0002(9)	0.017(1)
Mn(1)	2c	$\frac{1}{2}$	0	0	0.013(2)
Mn(2)	2d	$\frac{1}{2}$	$\frac{1}{2}$	0	0.016(2)
O(1)	4e	0.4974(13)	0.2456(10)	0.0547(12)	0.021(3)
O(2)	4e	0.2185(10)	0.0409(7)	$-$0.2199(10)	0.016(2)
O(3)	4e	$-$0.2613(13)	0.5062(9)	0.2566(13)	0.010(2)

Let us mention that monoclinic space groups $I2/b$ and $P2_1/a$ (or equivalent notations for other unit-cell settings) have already been used for structural descriptions of lacunar and substituted LMO phases. For instance, Maignan *et al.* (10) have described the crystal structure of a La$_{0.9}$MnO$_{3-\delta}$ powder sample in $I2/a$ group, Huang *et al.* (9) this of LaMnO$_3$ powder samples at low temperature in $P2_1/a$, and Mitchell *et al.* (22) this of La$_{1-x}$Sr$_x$MnO$_{3-\delta}$ compounds in $P2_1/c$. Recently, from TEM studies of epitaxial La$_{1-x}$Ca$_x$MnO$_{3-\delta}$ thin films deposited on SrTiO$_3$ substrate, Lebedev *et al.* (23) concluded to a monoclinic phase of $P2_1/c$ space group.

Although structures belonging to $R\bar{3}c$, $I2/b$, *Pnma*, and $P2_1/a$ space groups could be supposed quite different, examinations of their corresponding atomic structure reveal only small differences. The Glazer nomenclature allowing one to compare distortions of a cubic perovskite by octahedra tilting (Table 2), also yields insights into transformations between space groups. For instance, the tilt system is $a^-a^-a^-$ for the rhombohedral $R\bar{3}c$ perovskite structure, and $a^-b^-a^-$ for the monoclinic $I2/b$. The only difference of the octahedra tilting between these two space groups is the

tilt magnitude about the y axis which is different from those about the x and z axes. For *Pnma*, the tilt symbol being $a^-b^+a^-$ (or $a^-a^+a^-$), the octahedra along the y axis are tilted *in-phase*. For $P2_1/a$, the tilt system is the same as for

TABLE 5
Mn−O and La−O Near Neighbors Distances and Mn−O−Mn Angles

Bounds	Number	Distance (Å)	Average distance	Mn−O−Mn angles (°)	
(1) as-deposited film					
Mn−O(1)	2	1.948(2)		Mn−O(1)−Mn	170.5(5)
Mn−O(2)	2	1.924(5)		Mn−O(2)−Mn	162.7(5)
"	2	2.004(6)	1.959{41}		
La−O(1)	2	2.750(2)			
"	1	2.913(9)			
"	1	2.594(9)			
La−O(2)	2	2.507(7)			
"	2	2.579(7)			
"	2	2.922(8)			
"	2	2.994(8)	2.751{192}		
(2) Annealed film					
(a) Major phase, $I2/b$ space group					
Mn−O(1)	2	1.901(1)		Mn−O(1)−Mn	179.5(5)
Mn−O(2)	2	1.940(6)		Mn−O(2)−Mn	174.1(5)
"	2	1.985(6)	1.942{42}		
La−O(1)	2	2.744(2)			
"	1	2.723(9)			
"	1	2.764(9)			
La−O(2)	2	2.669(7)			
"	2	2.681(7)			
"	2	2.809(8)			
"	2	2.821(8)	2.745{60}		
(b) Minor phase, $P2_1/a$ space group					
Mn(1)−O(1)	2	1.929(4)		Mn(1)-O(2)-Mn(1)	156.9(5)
Mn(1)−O(2)	2	1.974(7)		Mn(1)-O(1)-Mn(2)	162.4(5)
"	2	1.986(8)	1.963{30}		
Mn(2)−O(1)	2	1.997(6)		Mn(1)-O(1)-Mn(2)	162.4(5)
Mn(2)−O(3)	2	1.924(7)		Mn(2)-O(3)-Mn(2)	175.0(5)
"	2	1.960(8)	1.960{37}		
La−O(1)	1	2.444(7)			
"	1	2.846(8)			
"	1	2.674(7)			
"	1	3.047(9)			
La−O(2)	1	2.874(9)			
"	1	3.118(9)			
"	1	2.331(8)			
"	1	2.772(8)			
La−O(3)	1	2.848(10)			
"	1	2.679(9)			
"	1	2.682(9)			
"	1	2.709(11)	2.752{222}		

Note. For the average distances, the numbers given between braces correspond a statistical deviation of distances observed in the same polyhedron; a large deviation means a large distortion of the polyhedron.

Pnma ($a^- b^+ a^-$) but $P2_1/a$ is a subgroup of *Pnma*; the only Mn site in *Pnma* is consequently splitted in two Mn sites in $P2_1/a$, such that two types of tilting and distortion can be observed for Mn octahedra. Therefore the crystal structures described either in $I2/b$ or $R\bar{3}c$ appear to be closely related, as well as those described either in $P2_1/a$ or *Pnma*.

The orthorhombic *Pnma* crystal structure is generally observed in pure and substituted LMO crystals exhibiting a low $Mn^{4+}/(Mn^{3+} + Mn^{4+})$ ratio (< 0.12 about), a Jahn–Teller distortion on octahedral Mn sites, an antiferromagnetic structure with a low superimposed ferromagnetic mode at low temperature and no insulator–metal transition (21). Such properties are always related to quite low magnetic ordering temperatures (in a T range of [120–200 K]). The rhombohedral $R\bar{3}c$ structure is observed in LMO crystals exhibiting a higher $Mn^{4+}/(Mn^{3+} + Mn^{4+})$ ratio (0.2–0.3), no Jahn–Teller distortion, a ferromagnetic structure at low temperature, and quasi-simultaneous semiconductor–metal and para-ferromagnetic transitions at temperatures close to a maximum of magnetoresistance (22). In this case, such properties are related to higher magnetic ordering temperatures (in a T range of [230–300 K]). However, from the physical properties observed in our films before and after annealing (12) it appears that a monoclinic $I2/b$ structure exhibits properties similar to those of $R\bar{3}c$ (which is consistent with a monoclinic $I2/b$ structure derived from the $R\bar{3}c$ space group).

Oxidization of LMO film by annealing in air reduces the oxygen deficiency δ and increases the $Mn^{4+}/(Mn^{3+} + Mn^{4+})$ ratio (its maximal value can be 0.6 for a stoichiometric compound $La_{0.8}MnO_3$). A charge ordering transition might be expected for a ratio value of 0.5. For instance, the substituted lanthanide manganite $Pr_{0.5}Ca_{0.5}MnO_3$ (23) exhibits a charge order transition corresponding to a pseudo tetragonal deformation developping from 250 K down to a temperature of antiferromagnetic transition at $T_N = 170$ K. Thus, because of the presence of two Mn sites in the $P2_1/a$ space group, charge and orbital partial ordering can be assumed in the annealed film. Average Mn–O distances are about the same on both Mn sites (1.96 Å), but the octahedra distortions are different (Table 5). The Mn(2) octahedron is tetragonally elongated (Mn–O distances are 2.00 Å along the **b** axis and 1.93 and 1.96 Å in the **ac** plane) while the Mn(1) octahedron is slightly tetragonally contracted (1.93 Å along the **b** axis and 1.97 and 1.98 Å in the **ac** plane). Actually, such distortions are indicative of Mn^{3+} and Mn^{4+} cations, respectively. Therefore it can be proposed that the minor $P2_1/a$ phase formed by annealing has probably a composition close to $La_{0.8}MnO_{2.95}$ ($Mn^{4+}/(Mn^{3+} + Mn^{4+}) = 0.5$) with a charge and orbital partial ordering.

Before and after annealing, both majority phases belong to the $I2/b$ space group. Interatomic distances observed in the as-deposited film are comparable to those of a powder sample A_2 prepared by Maignan *et al.* (10) at 1300°C and annealed at 1000°C, which presents a temperature of magnetic transition close to this of our as-deposited films (i.e., 220 K). XANES spectroscopy experiments performed on similar thin films showed that the $Mn^{4+}/(Mn^{3+} + Mn^{4+})$ ratio increases of about 25% after annealing (25). Therefore, comparisons must be made between MnO_6 octahedron distortions before and after thermal treatment. From crystallographic data gathered in Table 5, the Mn octahedron becomes after annealing more regular with a shorter average Mn–O distance (i.e., from 1.969 Å down to 1.942 Å). Besides, all the Mn–O–Mn bond angles, playing a key role in the superexchange and double exchange magnetic interactions, increase; Mn–O(1)–Mn and Mn–O(2)–Mn angles increase from 168.7° up to 179.5° and from 157.9° up to 174.1°, respectively. In this case, the augmentation of magnetic and electrical transition temperatures after annealing is in agreement with an increase of Mn–O–Mn angles, as expected for La-manganites (26). However, as such large bond angles (very close to 180°) have never been observed in bulk LMO materials with similar $Mn^{4+}/(Mn^{3+} + Mn^{4+})$ ratio, they might be assumed to be connected to strain effects from the MgO substrate.

The proportion of vacancies observed on cation sites could also be related to strain effects from the substrate. According to van Roosmalen *et al.* (27), the range of composition corresponding to the formation of the bulk $LaMnO_3$ perovskite phase at 900°C in air is in between $La_{0.908}MnO_3$ and $La_{1.202}MnO_{3+\delta}$ (or $LaMn_{0.832}O_3$). In this case, metal vacancies are usually observed on both La and Mn sites. The chemical formula of our films $La_{0.80}Mn_{1.00}O_{3-\delta}$ is outside this range of composition and there are no vacancies on Mn sites. Such a difference between thin film and bulk materials might be attributed to a strain effect of the substrate. In fact, using atomistic simulation techniques based on energetics cation migration in $LaMnO_3$ perovskite, De Souza *et al.* (28) showed that oxidative nonstoichiometry leads to the formation of cation vacancies on both La and Mn sites, although tending toward more La vacancies. They have also shown that structural changes toward a cubic symmetry are related to an increase of vacancies on La site. Now as mentionned above the Mn octahedra are much less distorted and the Mn–O–Mn are much closer to 180° in thin films than in bulk materials (the average crystal structure in thin film is cubic). Therefore, the structural properties of $LaMnO_3$ thin films would be related to vacancies only on La sites.

Finally, the surprising feature that the MgO substrate exhibits a structural transformation when in contact with a LMO layer was assumed to be the result of a strain rather than a chemical diffusion (cf. Section 3). The reason is that such a structural transformation was only observed in the case of the epitaxy of the $I2/b$ structure of LMO films before and after annealing and not in the case of the $P2_1/a$

TABLE 6
Transformation of the Atomic Coordinates between MgO Structures of Space Group: $Fm\bar{3}m$, $Fd\bar{3}$ and $Fd\bar{3}m$

$Fm\bar{3}m$				$Fd\bar{3}$	
Mg	$4a$	0, 0, 0	Mg(1)	$16c$	$\frac{1}{8}, \frac{1}{8}, \frac{1}{8}$
			Mg(2)	$16d$	$\frac{5}{8}, \frac{5}{8}, \frac{5}{8}$
O	$4b$	$\frac{1}{2}, \frac{1}{2}, \frac{1}{2}$	O	$32e$	$\frac{3}{8}+u, \frac{3}{8}+u, \frac{3}{8}+u$

structure. Then a change in the MgO atomic arrangement must be interpreted from a change of space group $Fm\bar{3}m$-to-$Fd\bar{3}$ (or $Fd\bar{3}m$). The atomic coordinates of the $Fm\bar{3}m$ MgO structure can equivalently be expressed in the $Fd\bar{3}$ space group (Table 6) where the Mg site splits into two sites and the oxygen site remains on one Wyckoff site with new coordinates ($\frac{3}{8}, \frac{3}{8}, \frac{3}{8}$). (The $Fd\bar{3}m$ space group does not need to be considered as it yields a same solution). A simple transformation of the MgO structure consists in a slight modification of the oxygen coordinates just by adding (or subtracting) a value u (i.e., $\frac{3}{8}+u$, $\frac{3}{8}+u$, $\frac{3}{8}+u$). A consequence of such a transformation is that the first neighbor atomic distances Mg–O are different between both Mg(1) and Mg(2) sites.

V. CONCLUSION

Crystal structure transformations of a magnetoresistive $La_{0.8}MnO_{3-\delta}$ thin film were studied with success using a conventional 4-circles diffractometer ordinarily designed for studies on bulk single crystals. From TEM observations and X-Ray diffraction measurements, the crystal structure of $La_{0.8}MnO_{3-\delta}$ thin films has been determined before and after annealing. In both cases, the crystal structure is monoclinic with a predominant space group $I2/b$ and twinned in microdomains. After annealing, changes of magnetic and electrical properties were interpreted on the basis of structural transformations determined in the phase of $I2/b$ space group; The formation of a minor monoclinic phase of $P2_1/a$ space group was also identified and interpreted as a charge ordered phase. In particular, it was shown that, as a result of annealing, the $Mn^{4+}/(Mn^{3+} + Mn^{4+})$ ratio increases and the Mn–O–Mn bond angles become close to $180°$. These structural changes lead to stronger magnetic interactions, a higher Curie temperature, and an improved magnetoresistance.

REFERENCES

1. E. O. Wollan and W. C. Koehler, *Phys. Rev.* **100,** 545 (1955).
2. W. C. Koehler and E.O. Wollan, *J. Phys. Chem. Solids* **2,** 100 (1957).
3. C. Zener, *Phys. Rev.* **82,** 403 (1951).
4. P. G. de Gennes, *Phys. Rev.* **118,** 141 (1960).
5. R. von Helmolt, J. Wecker, B. Holzapfel, L. Schultz, and K. Samwer, *Phys. Rev. Lett.* **71,** 2331 (1993); S. Jin, T. H. Tiefel, M. McCormack, R. A. Fastnacht, R. Ramesch, and L. T. Chen, *Science* **264,** 413 (1994).
6. J. A. M. van Roosmalen, P. van Vlaanderen, and E. H. P. Cordfunke, *J. Solid State Chem.* **114,** 516 (1995).
7. P. Norby, I. G. Krogh Andersen, and E. Krogh Andersen, *J. Solid State Chem.* **119,** 191 (1995).
8. B. C. Hauback, H. Fjellvag, and N. Sakai, *J. Solid State Chem.* **124,** 43 (1996).
9. Q. Huang, A. Santoro, J. W. Lynn, R. W. Erwin, J. A. Borchers, J. L. Peng, and R. L. Greene, *Phys. Rev. B* **55,** 14987 (1997).
10. A. Maignan, C. Michel, M. Hervieu, and B. Raveau, *Solid State Comm.* **101,** 277 (1997).
11. J. Rodriguez-Carvajal, M. Hennion, F. Moussa, A. H. Moudden, L. Pinsard, and A. Revcolevschi, *Phys. Rev. B* **57,** R3189 (1998)
12. S. Pignard, H. Vincent, J. P. Senateur, and J. Pierre, *J. Appl. Phys.* **82,** 4445 (1997); *J. Alloys Comp.* **262,** 157 (1997).
13. S. Pignard, H. Vincent, J. P. Senateur, K. Fröhlich, and J. Souc, *Appl. Phys Lett.* **73,** 999 (1998).
14. S. Pignard, H. Vincent, J. P. Senateur, and P. H. Giauque, *Thin Solid Films* **347,** 161 (1999).
15. J. P. Senateur, F. Weiss, O. Thomas, R. Madar, and A. Abrutis, French Patent no. 93/08838 PCT, FR9400858.
16. A. M. Glazer, *Acta Crystallogr. Sect. B: Struct. Sci.* **28,** 3384 (1972); *Acta Crystallogr. Sect. B: Struct. Sci.* **31,** 756 (1975).
17. P. M. Woodward, *Acta Crystallogr. Sect. B: Struct. Sci.* **53,** 32 (1997); *Acta Crystallogr. Sect. B: Struct. Sci.* **53,** 44 (1997).
18. C. J. Howard, *Acta Crystallogr. Sect. B: Struct. Sci.* **54,** 782 (1998).
19. G. M. Sheldrick, *Acta Crystallogr. Sect. A: Found Crystallogr.* **46,** 467 (1990); *J. Appl. Crystallogr.* (1993).
20. P. Wolfers, *J. Appl. Cryst.* **23,** 554 (1990).
21. F. Moussa, M. Hennion, J. Rodriguez-Carvajal, and H. Moudden, *Phys. Rev. B* **54,** 15149 (1996).
22. J. F. Mitchell, D. N. Argyriou, C. D. Potter, D. G. Hinks, J. D. Jorgensen, and S. D. Bader, *Phys. Rev. B* **54,** 6172 (1996).
23. O. I. Lebedev, G. Van Tendeloo, S. Amelinckx, B. Leibold, and H.-U. Habermeier, *Phys. Rev. B* **58,** 8065 (1998)
24. S. Pignard, thesis 1997/INPG/0189, ANRT Grenoble, 72672; S. Pignard, H. Vincent, M. Audier, J. Kreisel, G. Metellus, J. P. Senateur, and J. Pierre, "Nano-crystalline and Thin Film Magnetic Oxides" (I. Nedkov and M. Ausloos, Eds.), Kluwer Academic, Dordrecht, 1999.
25. Z. Jirak, F. Damay, M. Hervieu, C. Martin, B. Raveau, G. André, F. Bourée, *Phys. Rev. B* **61,** 1181 (2000).
26. M. Blamire and J. Evetts, *Phys. World* **20** (May 1996).
27. J. A. M. van Roosmalen, P. van Vlaanderen, and E. H. P. Cordfunke, *J. Solid State Chem.* **114,** 516 (1995); J. A. M. van Roosmalen and E. H. P. Cordfunke, *J. Solid State Chem.* **110,** 106 (1994).
28. R. A. De Souza, M. S. Islam, and E. Ivers-Tiffée, *J. Mater. Chem.* **9,** 1621 (1999).